17. D. Vanmaekelbergh and J. J. Kelly, *This Journal*, **136**, 108 (1989).
18. D. Vanmaekelbergh, Ph.D. Thesis, Univ. of Gent (1984).
19. A. Etcheberry, J. Gautron, E. M. Khoumri, and J. L. Sculfort, *J. Electroanal. Chem.*, **283**, 177 (1990).
20. P. H. L. Notten, *This Journal*, **131**, 2641 (1984).
21. S. R. Morrison and T. Freund, *J. Chem. Phys.*, **47**, 1543 (1967).
22. H. H. Goossens and W. P. Gomes, *This Journal*, **138**, 1696 (1991).
23. H. C. Gatos and M. Lavine, in "Progress in Semiconductors," Vol. 9, A. F. Gibson and R. E. Burgess, Editor, Temple Press, London (1965).

Theoretical and Experimental Investigations of Chlorine RF Glow Discharges

I. Theoretical

Eray S. Aydil[1] and Demetre J. Economou

Department of Chemical Engineering, University of Houston, Houston, Texas 77204-4792

ABSTRACT

A comprehensive model of chlorine plasma etching of polysilicon in a parallel plate reactor was developed. The Boltzmann transport equation and a bulk plasma model were used to calculate the rate coefficients of electron impact reactions. These coefficients were then used in a transport and reaction model to calculate the atomic chlorine concentration distribution. The same methodology may be applied to other plasma systems as well. Theoretical results for an empty reactor (no polysilicon film) are presented in this paper. Unified plots were developed which relate the electron density, self-sustained electric field, and electron impact coefficients in the bulk plasma to pressure, power, and reactor geometry. The calculated atomic chlorine concentration showed similar dependence on pressure and electrode spacing for either first or second order surface recombination kinetics. Experimental verification of the model predictions is presented in the accompanying paper.

Chemically reactive gas plasmas are used widely for manufacturing of integrated circuits, especially for etching and deposition of thin films (1). For example, chlorine and chlorine-containing plasmas are used to etch polysilicon, aluminum, and compound semiconductors (2). Despite the wide use of plasma processes, plasma reactor design continues to rely heavily upon trial-and-error procedures. The operating conditions, such as pressure, power, gas flow rate, and gas composition are varied in an empirical fashion until the process performance is satisfactory. This empirical approach is taken because of the complexity of the plasma and the intricate coupling of different physicochemical phenomena. When a satisfactory design is thus identified, however, it is invariably difficult to scale to new processes or levels of performance. Mathematical models can provide more rational methods for reactor design, and can be used for process optimization and control. The models must be tested with experimental data obtained under well-characterized conditions in order to improve accuracy and extend the range of validity.

There are a variety of phenomena affecting the outcome of a plasma process (3,4). Both charged and neutral particle transport and reaction, potential distribution in the plasma and in the sheath, and plasma-surface interactions strongly influence reactor behavior. Recently there has been emphasis on plasma reactor modeling and diagnostics in order to improve our understanding of reactive gas plasmas, and to develop more rational procedures for plasma reactor design. Several investigators have conducted modeling and/or experimental studies of low-pressure plasma systems (5-23). In each of these investigations, different aspects of the problem were emphasized. Graves (8) simulated an electropositive discharge using a continuum model with emphasis on the discharge structure and physics. Boeuf (9) studied an electronegative RF discharge, whereas Tsai and Wu (10) modeled two-dimensional RF discharges in nitrogen and sulfur hexafluoride. Kushner (11) and Cleland and Hess (12) emphasized the discharge chemistry, while Dalvie *et al.* (13-14), Folta and Alkire (15), Kao and Stenger (16), Kobayashi *et al.* (17), and Venkatesan *et al.* (18) emphasized neutral transport and reaction phenomena. Other investigators focused on understanding the plasma sheath and ion bombardment of surfaces (6, 19, 20). Kline and Kushner (21), and Graves (22) reviewed recent experimental and theoretical efforts in plasma processing.

Recently, Economou and Alkire (23), and Economou *et al.* (24) combined submodels describing the different aspects of the plasma reactor into an overall engineering model. Similar approaches have been taken by other researchers (25). However, a detailed analysis of the bulk plasma was not included. In the present study, a detailed description of the bulk plasma is included in an overall plasma reactor model.

Besides being a system of industrial importance, chlorine plasmas have been studied to some extent and there is a reasonable amount of information in the literature concerning the dominant species and reactions (26-30). Furthermore, chlorine plasmas involve a simple gas where polymerization does not occur. The chlorine plasma was chosen to elucidate the coupling between electron kinetics and neutral transport and reaction in plasma reactors. However, the general method of approach followed in this study may be applied to other plasma systems as well.

A model of the Cl_2 plasma etching of polysilicon was developed from first principles and was tested experimentally using various plasma diagnostics. The experimental and modeling approach is shown in Fig. 1. The overall model can be conceptually separated into four different submodels: the Boltzmann transport model, the bulk plasma model, the sheath model, and the etchant transport and reaction model. The electron energy distribution function, electron impact reaction rate coefficients, and electron transport properties, were determined by solving the Boltzmann transport equation. The time-dependent electron density and self-sustained electric field were calculated using an extension of the bulk plasma model developed by Rogoff *et al.* (26). The time-averaged reaction rate coefficients and electron density were subsequently used in a neutral transport and reaction model to determine the etchant concentration profiles, etch rate of polysilicon, and uniformity of etching. The predictions of the submodels, and of the overall model, were compared with experimental measurements. In general, the four sub-

[1] Present address: AT&T Bell Laboratories, Murray Hill, NJ 07974-2070.

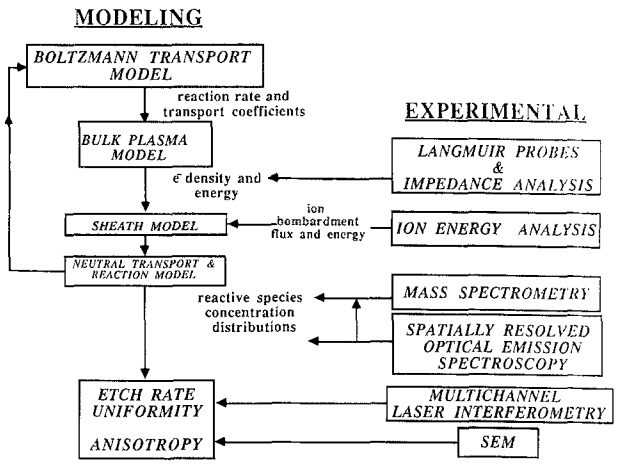

Fig. 1. Organization of the modeling and experimental studies.

models are coupled with one another. For example, the neutral transport and reaction model provides the gas composition, which in turn affects the electron energy distribution function. The latter affects the electron impact reaction rate coefficients, and therefore the plasma gas composition.

In this paper, theoretical results are presented for an empty reactor (no wafer with polysilicon film present). The corresponding experimental results and comparison with the model predictions are presented in the accompanying paper (Ref.(31), hereafter to be referred to as Part II). Analysis of polysilicon etching will be reported elsewhere.

Mathematical Model

A mathematical model for a chlorine plasma sustained in a parallel plate reactor was developed. A schematic of the reactor is shown in Fig. 2. The feedstock gas enters the reactor uniformly through a showerhead electrode and is dissociated into reactive radicals as the gas flows radially outwards. The radicals are transported by diffusion and convection, and participate in both homogeneous and heterogeneous reactions. Positive and negative ions as well as electrons are also created by electron impact of the neutrals.

Key internal plasma properties including electron energy and density, concentration distribution of charged and neutral species, and ion bombardment energy and flux cannot be controlled independently, but are determined instead by the reactor operating conditions. These plasma properties, in turn, determine the process outcome, such as etch rate, etch profile (anisotropy), uniformity, and selectivity. In this paper, key internal plasma properties are calculated as a function of operating conditions (such as the reactor geometry, pressure, gas flow rate, and power) in an empty reactor.

In order to reduce the problem to a computationally manageable level, it is necessary to introduce certain assumptions. Inevitably, the assumptions limit the range of operating conditions for which the model is valid. In the present case the model is valid for high pressures (>0.25 Torr), intermediate excitation frequencies (3-20 MHz), and large electrode gaps (>1.0 cm). The specific assumptions pertaining to each submodel are discussed separately with the development of that submodel. Further refinements of the model should concentrate on relaxing the assumptions while keeping the general methodology.

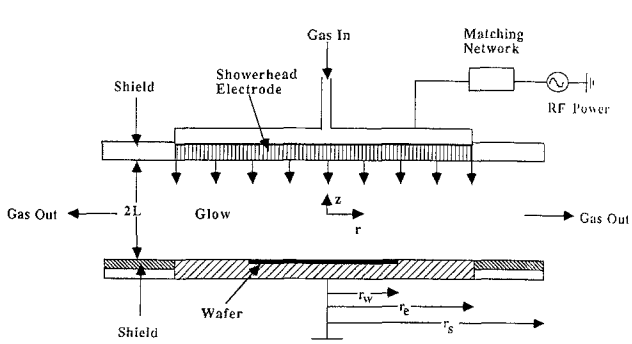

Fig. 2. Schematic of the single wafer plasma etching reactor studied.

Table I. Important reactions in the chlorine discharge.

Atomic ionization	$Cl + e^- \rightarrow Cl^+ + 2e^-$	[R1]
Molecular ionization	$Cl_2 + e^- \rightarrow Cl_2^+ + 2e^-$	[R2]
Dissociative attachment	$Cl_2 + e^- \rightarrow Cl_2^{-*} \rightarrow Cl^- + Cl$	[R3]
Dissociative excitation	$Cl_2 + e^- \rightarrow Cl_2^*(C^1\Pi) + e^- \rightarrow 2Cl + e^-$	[R4]
Dissociative ionization	$Cl_2 + e^- \rightarrow Cl^+ + Cl + 2e^-$	[R5]
Other electronic excitations	$Cl_2 + e^- \rightarrow Cl_2^*(B^3\Pi, 2^1\Pi \text{ and } 2^1\Sigma) + e^-$	[R6]
	$Cl + e^- \rightarrow Cl^* + e^-$	[R7]
Vibrational excitation	$Cl_2 + e^- \rightarrow Cl_2^* + e$	[R8]
Volume recombination	$Cl + Cl + M \rightarrow Cl_2 + Cl$	[R9]
Wall recombination	$Cl + \text{wall} \rightarrow \frac{1}{2} Cl_2$	[R10]

Boltzmann transport model.—The electron energy distribution function (EEDF) plays a central role in determining the plasma chemistry and kinetics. The mean electron energy, the electron transport coefficients, and the rate coefficients for electron impact reactions may be calculated from knowledge of the EEDF. The EEDF is often assumed to be Maxwellian because proper calculation of the EEDF is a problem of considerable complexity. A major difficulty is that the collision cross sections for electron impact reactions, especially for electron-radical collisions, are not known. Hence, in many plasma modeling works, key plasma properties, such as electron density and energy, are treated as adjustable parameters.

In this study the EEDF was obtained by solving the Boltzmann transport equation (32)

$$\left(\frac{\partial}{\partial t} + \mathbf{v} \cdot \nabla_{\mathbf{r}} - \frac{eE}{m_e} \cdot \nabla_{\mathbf{v}}\right) f(\mathbf{r}, \mathbf{v}, t) = \left(\frac{\partial f}{\partial t}\right)_{\text{collisions}} = S \quad [1]$$

The EEDF depends on the electric field, the gas density, and the nature of collisions that electrons undergo in the plasma. More specifically, the electric field to neutral density ratio, E/N, the plasma composition, and a set of collision cross sections are needed as input to the Boltzmann equation to evaluate the collision integral, S, and the EEDF. Electron collision processes considered in this work are given in Table I. Total ionization and attachment cross sections for molecular chlorine have been measured by Kurepa and Belic (33). Other collision cross sections have been estimated by Rogoff *et al.* (26). For the chlorine discharge, momentum transfer, molecular ionization, dissociative ionization, ion-pair formation, dissociative attachment, molecular excitations to $B^3\Pi$, $2^1\Pi$, and $2^1\Sigma$ states, dissociative excitation to $C^1\Pi$ state, vibrational excitations, atomic ionization, and atomic excitations were considered. Atomic excitation cross sections from Ganas (34) were used. A computer code developed by Morgan (35) was adopted to solve the Boltzmann transport equation. Morgan assumed that the EEDF was independent of position and used first order spherical harmonic expansion to solve the Boltzmann equation. The isotropic EEDF $f_0(\epsilon)$ is normalized using

$$\int_0^\infty \epsilon^{1/2} f_0(\epsilon)\, d\epsilon = 1 \quad [2]$$

A semilogarithmic plot of $f_0(\epsilon)$ *vs.* ϵ is a straight line for a Maxwellian distribution. This enables one to compare the calculated EEDF to a Maxwellian distribution. Details of the calculation, discussion of assumptions, and evaluation of the collision integrals can be found in Morgan's report (35) and references therein.

Once the EEDF is calculated, a number of important quantities, such as the electron drift velocity, rate coefficients for electron impact reactions, and the mean and characteristic electron energy can be computed (32,35). For example, the rate coefficients for reactions [R1]-[R4] of Table I are given by

$$k_j = \left(\frac{2e}{m_e}\right)^{1/2} \int_0^\infty f_0(\epsilon)\, \sigma_j(\epsilon)\, \epsilon\, d\epsilon \qquad [3]$$

In a pure chlorine discharge the reaction rate coefficients are functions of E/N and atomic chlorine mole fraction, y_1, since the EEDF is a function of these two variables.

Bulk plasma model.—For a given set of operating conditions, the bulk plasma model can predict the time-dependent self-sustained electric field as well as the electron density. Once the electric field waveform is known, the time-dependent electron impact reaction rate coefficients and electron energy can be found for a self-sustained discharge.

It was assumed that "beam electrons" which may be created by secondary processes at the electrode surface do not penetrate the bulk plasma. Hence, ionization by bulk electrons was assumed to be the dominant mechanism for electron production in the plasma. It was further assumed that the EEDF follows the instantaneous electric field (*i.e.* it is modulated completely). For this assumption to hold, the electron energy relaxation frequency, υ_u, must be higher than the applied radian frequency, ω. Flamm (36, 37) estimated υ_u for a Cl_2 discharge at 0.3 Torr to be about 63 MHz. The region in the E/N-N parameter space for which $\upsilon_u > \omega$ was calculated by Rogoff *et al.* (26). It was found that, for an atomic chlorine mole fraction of 0.4 and E/N = 190 Td, $\upsilon_u = \omega$ at 0.4 Torr, and $\upsilon_u < \omega$ below 0.4 Torr. Hence the approximation that the EEDF is modulated by the applied frequency does not appear as good at low pressures. Fortunately, as pressure is lowered below 0.4 Torr, electron diffusion losses become significant and cause the self-sustained E/N to increase well above 190 Td, increasing the electron energy relaxation frequency as well.

At high pressures (more accurately for high values of $N\Lambda$, see Results and Discussion) the electron balance is dominated by single-step ionization of molecular and atomic chlorine, and attachment to molecular chlorine (26). At low pressures, electron loss by diffusion and drift to the walls becomes significant compared to attachment. Recent distributed parameter continuum models of the chlorine discharge have shown that the electron density and energy, as well as the electric field, are uniform in the bulk plasma and change rapidly only across a very thin sheath next to the electrode surface (38). This uniformity in electron density is a result of reduced space charge effects in the bulk plasma due to the large density of negative ions, Cl^-. Hence, a time-dependent lumped parameter model can be used to calculate the electron density and energy, and the bulk electric field. In this model, the charged particle density and the electric field are assumed to be spatially uniform in the bulk plasma. The electron balance can be written as

$$\frac{dn_e}{dt} = (k_{i1}\, y_1 + (k_{i2} - k_a)\, y_2)\, N\, n_e - \frac{D_{ae}}{\Lambda^2} n_e \qquad [4]$$

The terms on the right hand side of Eq. [4] account for electron production by atomic (rate coefficient k_{i1}) and molecular (k_{i2}) ionization, and electron loss by attachment (k_a) and diffusion, respectively. For the reactor configuration used in this study the characteristic diffusion length, Λ, was taken as

$$\frac{1}{\Lambda^2} = \left(\frac{2.405}{r_e}\right)^2 + \left(\frac{\pi}{2L}\right)^2 \qquad [5]$$

An expression for the ambipolar diffusion coefficient of electrons in a gas discharge containing an arbitrary mixture of charged species has been derived by Rogoff (39). For a discharge with three types of charged species (negative ions, positive ions, and electrons), and with a high ratio of ion to electron density ($\chi = n_+/n_e >> 1$), the electron ambipolar diffusion coefficient can be approximated by

$$D_{ae} = D_e \left(\frac{\chi}{\mu_r + \chi}\right) \qquad [6]$$

where $\mu_r = \mu_e/(\mu_+ + \mu_-)$, and D_e is the free electron diffusivity. If one also has $\chi >> \mu_r$, the electrons diffuse freely in a sea of neutrals and ions. Under the conditions examined in this work, χ was between 50 and 300, and μ_r was estimated to be 200. The electron diffusion coefficient was determined from the EEDF. Then the ambipolar diffusivity was estimated to be 10^6 cm^2/s at 1 Torr and 300 K. Furthermore, the product of the diffusion coefficient and neutral density was taken to be constant. The plasma temperature was assumed to be independent of position and constant at 300 K (26, 27).

The positive and negative ions are too heavy to respond to the high frequency field and do not contribute appreciably to the current flowing through the plasma. The total current can therefore be approximated as the sum of the electron conduction current and the displacement current

$$I_t = eAn_e\, v_d + \epsilon_0 A \frac{dE}{dt} \qquad [7]$$

The total current was assumed to be sinusoidal

$$I_t = I_0 \sin(\omega t) \qquad [8]$$

where $\omega = 2\pi\upsilon_a$. The peak current, I_0, is related to the time-averaged power dissipated in the plasma by

$$\langle P_{RF} \rangle = \frac{2LI_0}{T} \int_t^{t+T} E(t)\, sin\, (\omega t)\, dt \qquad [9]$$

Due to the high resistivity of the bulk plasma in electronegative discharges, a large fraction of the power is dissipated in the bulk. The power dissipated in the sheaths, as estimated from experimental measurements of the ion bombardment flux and sheath voltage, was typically less than 10% of the total power and was neglected.

Equations [4] and [7] can be solved for the steady-state electric field and electron density waveforms by knowing either the peak current or the time-averaged power dissipated in the plasma. These equations were solved as an initial value problem until a periodic steady-state was reached. Using power as input, the peak current was found by a Newton-Raphson iteration.

At the steady state, the electric field varied periodically with a frequency equal to the applied frequency, while the electron density varied periodically with twice the applied frequency. The rate coefficients for reactions [R1]-[R4] of Table I, and the mean and characteristic electron energy are all functions of time through their dependence on E/N. The time-average of a quantity g was calculated by integrating over a period

$$\langle g\, (y_1) \rangle = \frac{1}{t} \int_t^{t+T} g(y_1, t)\, dt \qquad [10]$$

For example g can be n_e, k_a, k_d, ϵ_c, or T_e. The time-averaged quantities were used in the transport and reaction model and/or compared to experimental measurements. Such comparisons are made in Part II.

Neutral transport and reaction model.—The parallel plate plasma etcher shown in Fig. 2 is radially symmetric and a two dimensional (r, z) mathematical model is sufficient to describe the fluid velocity, etchant concentration, and etch rate profiles in the reactor. The momentum and mass balances were decoupled by assuming constant physical properties and negligible volume change upon re-

action. The pressure was high enough for the continuum approximation to be valid.

The gas velocity distribution was found by solving the continuity and Navier-Stokes equations

$$\nabla \cdot \mathbf{u} = 0 \quad [11]$$

$$\rho \mathbf{u} \cdot \nabla \mathbf{u} + \nabla \cdot \tau + \nabla P = 0 \quad [12]$$

The following boundary conditions were used

$$u = 0 \quad v = 0 \quad \text{at} \quad z = -L \quad \text{and} \quad 0 \le r \le r_s \quad [13]$$

$$u = 0 \quad v = -v_w \quad \text{at} \quad z = L \quad \text{and} \quad 0 \le r \le r_e \quad [14]$$

$$u = 0 \quad v = 0 \quad \text{at} \quad z = L \quad \text{and} \quad r_e \le r \le r_s \quad [15]$$

$$u = 0 \quad \frac{\partial v}{\partial r} = 0 \quad \text{at} \quad -L \le z \le L \quad \text{and} \quad r = 0 \quad [16]$$

$$u = u_{max}\left(1 - \left(\frac{z}{L}\right)^2\right), v = 0 \quad \text{at} \quad -L \le z \le L \quad \text{and} \quad r = r_s \quad [17]$$

where u and v are the radial and axial components of the velocity vector. The gas velocity at the showerhead v_w and the maximum velocity u_{max} are given by

$$v_w = \frac{Q}{\pi r_e^2}, \quad u_{max} = \frac{3}{8}\frac{v_w r_e^2}{L r_s} = \frac{3}{8}\frac{Q}{\pi L r_s} \quad [18]$$

Boundary conditions Eq. [13] and Eq. [15] imply no slip on the walls. Equation [14] is for a uniform gas entrance velocity at the showerhead electrode, and Eq. [16] is a result of radial symmetry. A well-developed parabolic velocity profile at the reactor exit was assumed (Eq. [17]). The gas viscosity was calculated using standard estimation techniques (40) and was found to be 140 μP at 300 K.

The Navier-Stokes and the continuity equations were solved using the penalty function formulation and the finite element method (FEM). The numerical solution was verified with an approximate solution (24). For low flow rates (<30 sccm), for which the Reynolds number is low ($1 > \mathrm{Re} = v_w L/2\upsilon$), the approximate solution described the flow field accurately and was subsequently used in the etchant mass balance.

In the absence of appreciable concentration of reaction products, the total gas concentration is

$$c_1 + c_2 = N = \frac{P}{k_B T_g} \quad [19]$$

where subscripts 1 and 2 refer to atomic and molecular chlorine, respectively. Moreover, the time constant for etchant reactions is much greater than the applied frequency. Thus, although the etchant production rate is modulated by oscillations of the electron energy, the steady-state etchant species concentration will assume a time-independent average value. Hence, no time dependence was included in the etchant mass balance.

Electron impact dissociation, reaction [R4], and dissociative attachment, reaction [R3], are two possible channels for production of atomic chlorine. Production of Cl via the latter reaction was estimated to be 20-40 times smaller than the former (26). Dissociative attachment is an important reaction for production of negative ions and loss of electrons, but is relatively unimportant for the production of Cl. In the absence of etchable material, atomic chlorine is removed from the reactor mainly by heterogeneous recombination reactions on the electrodes. During etching of a film (*e.g.*, polysilicon), the etching reaction also acts as a sink of atomic chlorine. At relatively high pressures, atomic chlorine is also eliminated via the homogeneous recombination reaction [R9], where M is a third body required to conserve momentum and energy in the collision. The reaction rate coefficient for [R9] was taken from Lloyd (41) (k_r in Eq. [20] is 9.0×10^{-32} cm^6/s-mol^2, twice the k value reported by Lloyd). The etchant mass balance can then be written as

$$-D_1 \nabla^2 c_1 + \mathbf{u} \cdot \nabla c_1 - \langle (2k_d + k_a) n_e \rangle c_2 + k_r c_1^2 c_M = 0 \quad [20]$$

The product of pressure and diffusion coefficient for atomic chlorine in molecular chlorine was estimated to be 75 Torr-cm^2/s at 300 K (37). The term in brackets is the time-averaged production rate coefficient of atomic chlorine calculated from Eq. [10]. This term couples the Boltzmann transport model, bulk plasma model, and etchant transport and reaction model. It should be noted that the production rate coefficient is a function of c_1 since the EEDF depends on c_1. Furthermore, c_1 is a function of position in the reactor, making the radical production rate coefficient spatially dependent. However, for small atomic chlorine mole fractions ($y_1 < 0.2$) the dependence of this coefficient on c_1 is weak and its effects are secondary (see results and discussion). Under this condition, the etchant production rate coefficient can be considered independent of position, and is then only a function of pressure, power, and reactor geometry.

Etching and wall recombination reactions enter the model through the boundary conditions

$$\frac{\partial c_1}{\partial r} = 0 \quad \text{at} \quad r = 0, r = r_s \quad \text{and} \quad -L < z < L \quad [21]$$

$$-D_1 \frac{\partial c_1}{\partial z} - v_w c_1 = R_w(c_1) \quad \text{at} \quad z = L \quad \text{and} \quad 0 < r < r_e \quad [22]$$

$$-D_1 \frac{\partial c_1}{\partial z} = R_w(c_1) \quad \text{at} \quad z = L \quad \text{and} \quad r_e < r < r_s \quad [23]$$

$$D_1 \frac{\partial c_1}{\partial z} = R_w(c_1) \quad \text{at} \quad z = -L \quad \text{and} \quad 0 < r < r_s \quad [24]$$

where R_w is the wall recombination rate (reaction [R10]) which depends on the wall material and surface condition. Heterogeneous recombination reaction kinetics is poorly understood. The reaction rate coefficient and even the mechanism of recombination may change with subtle changes of the surface condition. For example, Ogryzlo (42) found that the surface recombination rate coefficient depended on water contamination. The rate coefficients on the same material may differ from "day to day" (43), even when measured by the same investigator (44). Generally, wall recombination is assumed to obey first order kinetics, although second order and Langmuir-Hinshelwood kinetics have also been used (29). In this study a power law dependence was used, namely

$$R_w(c_1) = k_n c_1^n \quad [25]$$

where k_n is the nth order reaction rate coefficient. On surfaces undergoing etching boundary condition Eq. [24] is replaced by

$$D_1 \frac{\partial c_1}{\partial z} = R_w(c_1) + R_t(I_+, E_+, c_1) \quad \text{at} \quad z = -L \quad \text{and} \quad 0 < r < r_w \quad [26]$$

Sheath model.—Ion transport in the sheath is important because it affects the ion bombardment energy and flux, and in turn the etch rate and anisotropy through Eq. [26]. Ions are accelerated in the sheath, and, while doing so, suffer collisions, mainly with neutrals. These collisions reduce the ion bombardment energy to values below the sheath voltage. For frequencies above the ion transit frequency (1-3 MHz), ions do not respond to the instantaneous sheath electric field, and an equivalent dc sheath model may be used. Unfortunately, models of the electronegative sheath, especially in the collisional regime, are not well developed. Economou *et al.* (20) have considered an equivalent dc sheath model in the collisional regime.

The model couples the current continuity equation to the ion fluid equation of motion and to the Poisson equation for the potential distribution in the sheath. It was shown that, under conditions of interest in plasma etching, the dimensionless ion drift velocity and the dimensionless sheath potential are related by

$$(u_+^*)^2 = \frac{(-10\ V^*)^{2/5}}{(2\mathrm{Co})^{4/5}\,(1 + 2\ \mathrm{Co})^{1/5}} \qquad [27]$$

where the collision number is $\mathrm{Co} = 0.5\ N\lambda_D\ \sigma_t$, and the dimensionless variables are defined as follows

$$V^* = \frac{eV_s}{k_B T_e} \quad ; \quad u_+^* = u_+ \sqrt{\frac{m_+}{k_B T_e}} \qquad [28]$$

The model of Economou *et al.*, assumes Maxwellian electrons in the plasma, an assumption which does not hold for the chlorine plasma. However, the characteristic electron energy calculated from the EEDF was used as an "equivalent electron temperature." The mean ion bombardment energy (normal to the electrode) can be calculated from the drift velocity using

$$\overline{E}_+ = \left(\frac{1}{2} m_+ u_+^2\right) \qquad [29]$$

The sheath model does not take into account the presence of negative ions. This may be a poor approximation especially at low frequencies (< 1 MHz). Nevertheless, this model was used to obtain estimates of the mean ion energy. As shown in Part II, the model predicts the experimentally measured ion bombardment energy surprisingly well.

Results and Discussion

Boltzmann transport model.—The EEDF in the chlorine plasma was found to be nonMaxwellian for the range *E/N* 10-600 Td and mole fraction of atomic chlorine y_1 = 0-1 studied. For a given atomic chlorine mole fraction the EEDF is a function of *E/N* only. The EEDF for $y_1 = 0$ is shown in Fig. 3 for several values of *E/N*. The tail of the EEDF falls off rapidly as the high energy electrons are depleted via various inelastic collisions. As *E/N* increases, the EEDF becomes more Maxwellian-like (*i.e.* closer to a straight line). However nonMaxwellian behavior was still evident even at 500 Td.

The effect of atomic chlorine mole fraction on the EEDF at *E/N* = 200 Td is shown in Fig. 4. The tail of the EEDF rises as the atomic chlorine mole fraction in the plasma increases. This is because the momentum exchange cross section of atomic chlorine is smaller than that of molecular chlorine.

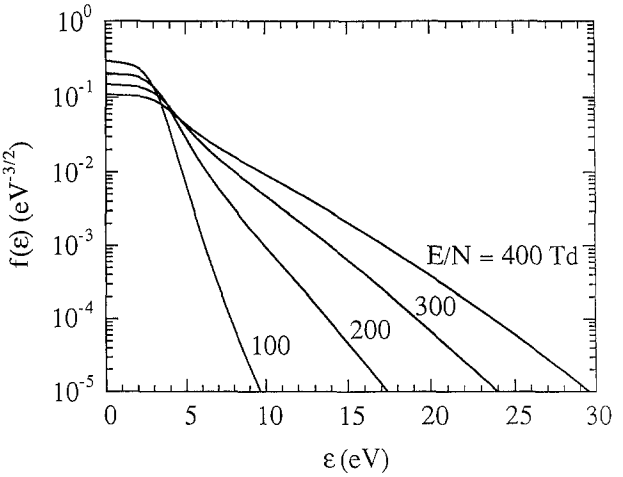

Fig. 3. Electron energy distribution function for different E/N and for atomic chlorine mole fraction equal to zero.

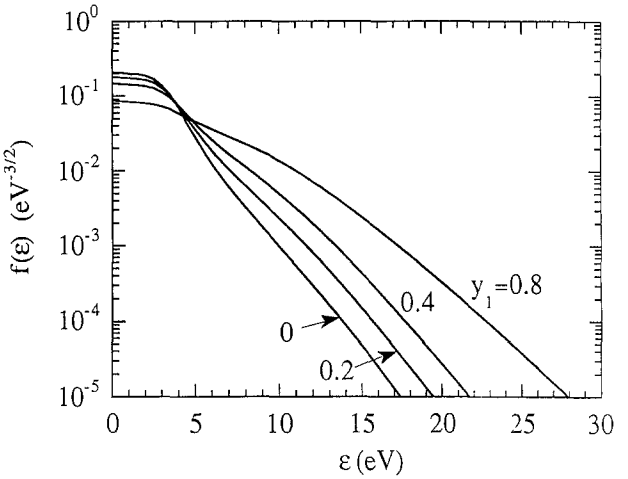

Fig. 4. Electron energy distribution function for different atomic chlorine mole fractions and *E/N* = 200 Td.

The mean electron energy and the electron impact reaction rate coefficients all increased with increasing *E/N* and increasing atomic chlorine mole fraction (with the exception of the attachment reaction). Figures 5 and 6 show the mean and characteristic electron energy as a function of *E/N* and atomic chlorine mole fraction, respectively. The characteristic energy is defined as the ratio of the electron diffusion coefficient to the electron mobility and is equal to 2/3 of the mean energy for a Maxwellian distribution.

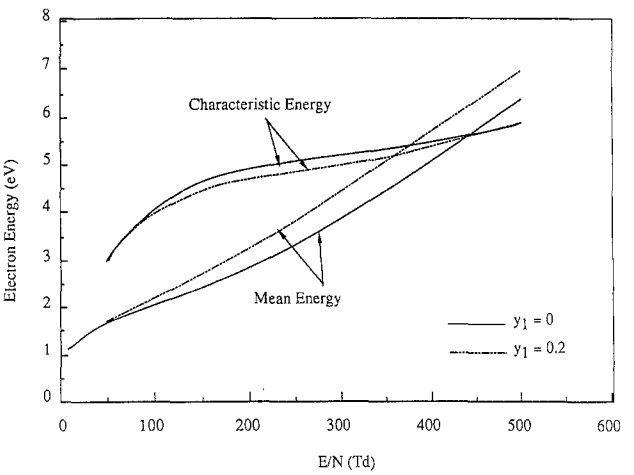

Fig. 5. Characteristic and mean electron energy as a function of *E/N* and for two atomic chlorine mole fractions.

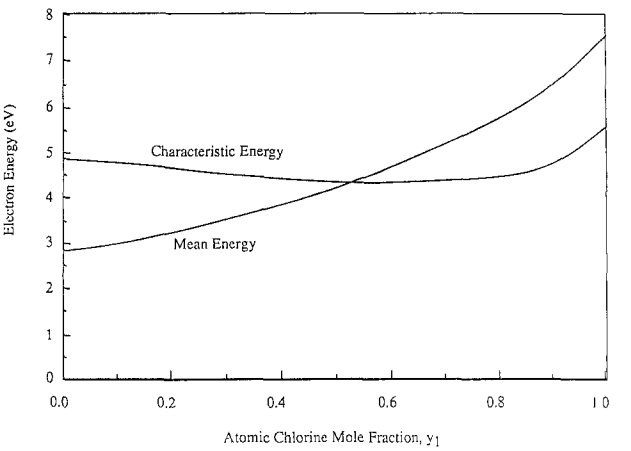

Fig. 6. Characteristic and mean electron energy as a function of atomic chlorine mole fraction and for *E/N* = 200 Td.

(For a Maxwellian distribution the electron temperature and characteristic energy are identical.) The nonMaxwellian character of the EEDF is also evident from Fig. 5, which shows that the characteristic energy is higher than the mean energy for *E/N* less than about 350 Td. As the atomic mole fraction increases, the characteristic energy decreases slightly, despite the fact that the mean energy increases. Figure 6 shows that the characteristic energy is relatively insensitive to the atomic chlorine mole fraction, whereas the mean energy increases monotonically with increasing atomic chlorine mole fraction.

The calculated total (molecular plus atomic) ionization and attachment rate coefficients were similar to the ones reported by Rogoff *et al.* (26), and are shown in Fig. 7(a). The attachment rate coefficient k_a is relatively insensitive to the electric field and Cl mole fraction, as would be expected for collision processes with low energy threshold. The calculated values of k_a varied between 1.6×10^{-10} and 2.2×10^{-10} cm^3/s, and exhibited a slight maximum as a function of *E/N*. The dependence of the electron impact dissociation (reaction [R4]) rate coefficient on *E/N* and Cl fraction is shown in Fig. 7(b). Reaction [R4] is the major channel by which atomic chlorine, the etchant species, is produced in the chlorine discharge.

It is convenient to develop analytic expressions for the various rate coefficients since the results of the Boltzmann transport model are used as input to the bulk plasma and neutral transport and reaction models. Frequently, the electron impact rate coefficients are represented as a function of the electron temperature by an Arrhenius-type equation (8)

$$k_j = k_{j0} \exp\left(-\frac{\epsilon_{act,j}}{k_B T_e}\right) \qquad [30]$$

where $\epsilon_{act,j}$ is the activation energy for reaction j (ionization potential for example). Attempts to fit the rate coefficients to the above equation were unsuccessful. Instead, the dissociation and ionization rate coefficients were found to follow an Arrhenius behavior as a function of *E/N* over the range 100-500 Td, which includes the *E/N* values of interest. The quality of the fit degraded at lower values of *E/N*. Semilogarithmic plots of k_d, k_{il}, and k_{i2} *vs.* the reciprocal of *E/N* were straight lines and the rate coefficients were expressed as

$$k_j = k_{j0} \exp\left(-\frac{(E/N)_{act,j}}{(E/N)}\right) \qquad [31]$$

where $(E/N)_{act,j}$ is the "activation electric field to neutral density ratio," the slope of the semilogarithmic plot of k_j *vs.* the reciprocal of *E/N*. The activation field and the preexponential factor depended on the atomic chlorine mole fraction (45).

The weak field limit of the calculated electron mobility and diffusivity values were 5.6×10^7 cm^2/V-s and 3.3×10^5 cm^2/s, respectively, for $y_1 = 0$ at 1 Torr and 300 K. (All the reported values of diffusivity and mobility are at 1 Torr, 300 K, unless noted otherwise.) The mobility decreased with increasing *E/N*, but was approximately constant at 2×10^5 cm^2/V-s (±15%) in the range 150-500 Td. The diffusivity exhibited a maximum at low *E/N* and then decreased from 2×10^6 cm^2/s at 10 Td to 10^6 cm^2/s at 150 Td (45). Above 150 Td, the diffusivity was approximately constant at 10^6 cm^2/s (±10%). For *E/N* greater than 50 Td, the drift velocity could be represented by a power law

$$v_d = a\left(\frac{E}{N}\right)^{\gamma} \qquad [32]$$

with a and γ depending on the atomic chlorine mole fraction (26, 45).

Bulk plasma model.—For a given reactor geometry, power, and pressure, the state of the bulk plasma was determined by calculating the electron density and self-sustained electric field waveforms (see Eq. [4] and Eq. [7]). Figure 8 shows the electron density, current, *E/N*, and

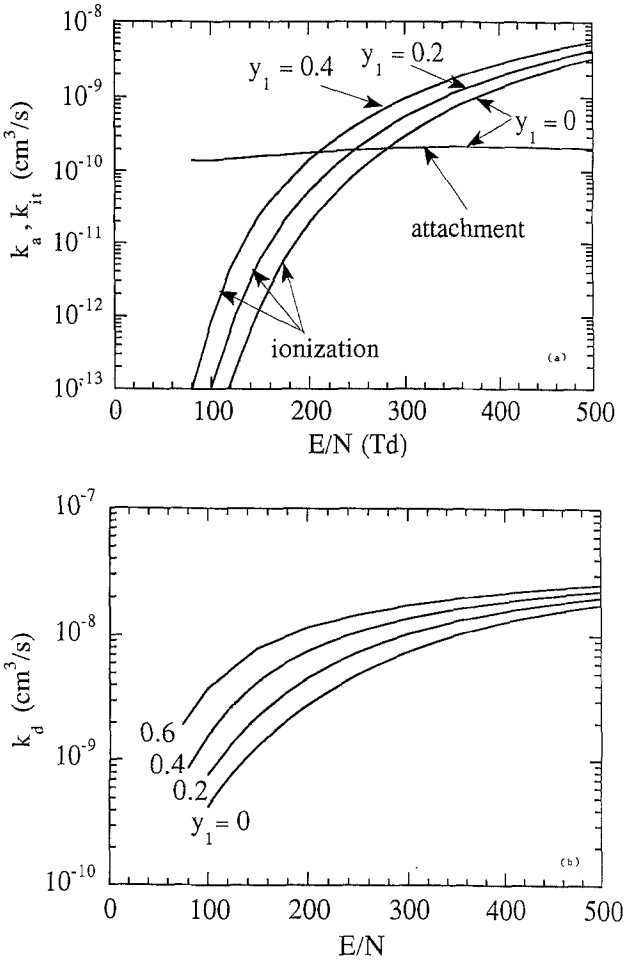

Fig. 7. (a) Attachment and total ionization rate coefficient as a function of *E/N*. (b) Electron impact dissociation rate coefficient as a function of *E/N*.

instantaneous power waveforms for two different conditions, namely, 1.5 Torr-50 W and 0.5 Torr-100 W. Current and *E/N* are nearly in phase for the low pressure-high power conditions (*i.e.*, for high electron density, Fig. 8(b), whereas the field leads the current by approximately 42° for the high pressure-low power conditions (*i.e.*, for low electron density, Fig. 8(a)). The electron density is modulated only slightly. The peak value of the time-varying electron density was generally less than 10% of the average value. The electron density and instantaneous power were not in phase. In fact, they can be nearly 90° out of phase when the electron density is low, as shown in Fig. 8(a). When current and field are in phase, the instantaneous power is always greater than zero (Fig. 8(b)) and the bulk plasma acts as a resistor. This result will be used to simplify the plasma impedance analysis in Part II.

There are a number of important internal plasma properties, including the time-averaged rate coefficients of electron impact reactions, electron energy and density, and rms electric field to neutral density ratio. It is convenient if these variables or groups containing the variables can be expressed as a unified function of a scaling parameter for a wide range of operating conditions. Examples of such unified scaling "laws" are given by Bell (46). For example, when $<n_e> \Lambda^2 > 10^9$ cm^{-1}, *E/N* and $(<n_e> V_p)/(<P_{RF}> \Lambda)$ become independent of electron density and are functions of $N\Lambda$ only (46). Thus plots of these groups as a function of $N\Lambda$ can be used to describe the state of the plasma.

It can be shown, by using an approximate solution to the bulk plasma model, that for a given mole fraction of atomic chlorine the following parametric groups are functions of $N\Lambda$ only

$$\left(\frac{E}{N}\right)_{rms} = F_1(N\Lambda) \qquad [33]$$

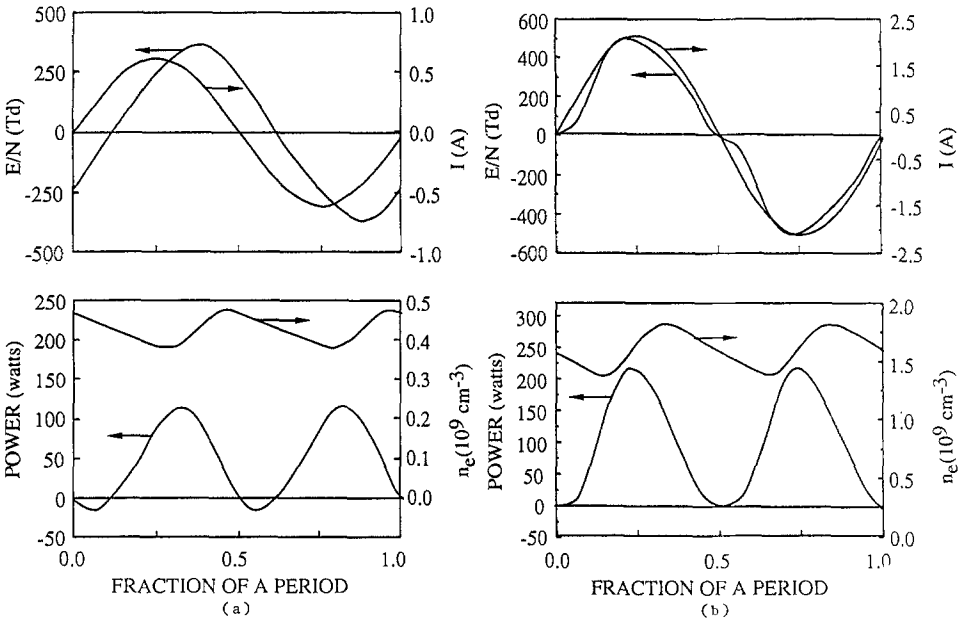

Fig. 8. Electric field, current, electron density, and instantaneous power waveforms for (a) 1.5 Torr, 50 W and (b) 0.5 Torr, 100 W. In both cases electrode spacing was 1.27 cm.

$$\frac{\langle n_e \rangle V_p}{\langle P_{RF} \rangle \Lambda} = F_2(N\Lambda) \quad [34]$$

$$\frac{I_0^2 V_p}{\langle P_{RF} \rangle \Lambda A^2 \langle n_e \rangle} = F_3(N\Lambda) \quad [35]$$

To test Eq. [33]-[35] and find the corresponding functional relationships, Eq. [4]-[9] were solved numerically for different values of power, pressure, and Λ. For each set of operating conditions the time-averaged rate coefficients, electron density and energy, rms E/N, and peak current were computed. It was found that the parametric groups shown on the left hand side of Eq. [33-35] were indeed unique functions of $N\Lambda$. The functional dependencies are shown in Fig. 9-12. Slight deviations from such functional dependencies were observed when the electron density was less than 7×10^8 cm^{-3}.

The dependence of $(E/N)_{rms}$ on $N\Lambda$ and atomic chlorine mole fraction is shown in Fig. 9. The electric field to neutral density ratio becomes independent of $N\Lambda$ above 2.0×10^{16} cm^{-2}, as the loss of electrons via diffusion becomes negligible compared to attachment. For high values of $N\Lambda$, the self-sustained electric field is determined solely by the dependence on E/N of the total ionization and attachment rate coefficients. Now, since atomic chlorine has a higher ionization threshold compared to molecular chlorine, it may be expected that a higher $(E/N)_{rms}$ is required for sustaining a plasma having a higher atomic chlorine concentration. Contrary to this expectation, the required $(E/N)_{rms}$ decreases with increasing atomic chlorine mole fraction. This is because the tail of the EEDF extends to higher electron energies with increasing atomic chlorine mole fraction, as seen previously (see Fig. 4). The longer tail causes an increase in the ionization rate coefficients, and shifts the intersection of the attachment rate coefficient with the total ionization rate coefficient towards lower E/N (see also Fig. 7a).

The dependence of electron density on operating conditions is shown in Fig. 10 in which the group $(\langle n_e \rangle V_p)/(\langle P_{RF} \rangle \Lambda)$ is plotted as a function of $N\Lambda$, for different y_1. At constant power and constant Λ, the electron density first increases with pressure, goes through a maximum, and then decreases with further increase in pressure. Figure 10 also shows that the electron density changes only moderately for moderate variations of the atomic chlorine mole fraction. Figure 11 shows a group containing I_0 as a function of the reciprocal of $N\Lambda$, for several atomic chlorine mole fractions.

Since the electron impact reaction rate coefficients are functions of E/N and y_1, their time-averaged values are functions of $N\Lambda$ only, for a given atomic chlorine mole fraction. The time-averaged dissociation rate coefficient was calculated using Eq. [10] and is shown in Fig. 12. The dissociation rate coefficient is relatively independent of operating conditions for high $N\Lambda$. However, $\langle k_d \rangle$ increases drastically at low $N\Lambda$ as the electron diffusion loss

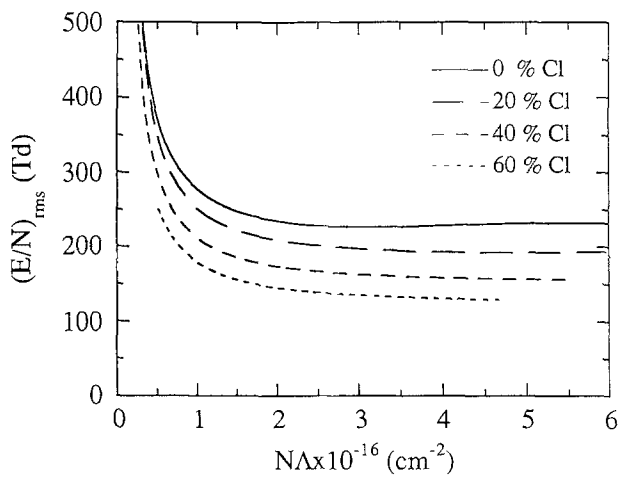

Fig. 9. Root mean square E/N as a function NΛ.

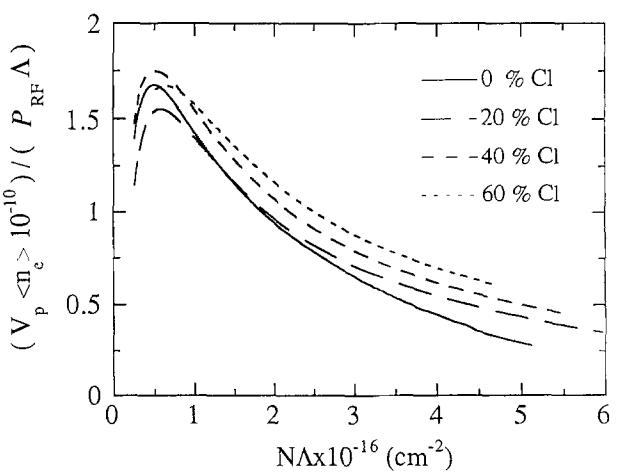

Fig. 10. $(V_p \langle n_e \rangle)/(\langle P_{RF} \rangle \Lambda)$ as a function of NΛ.

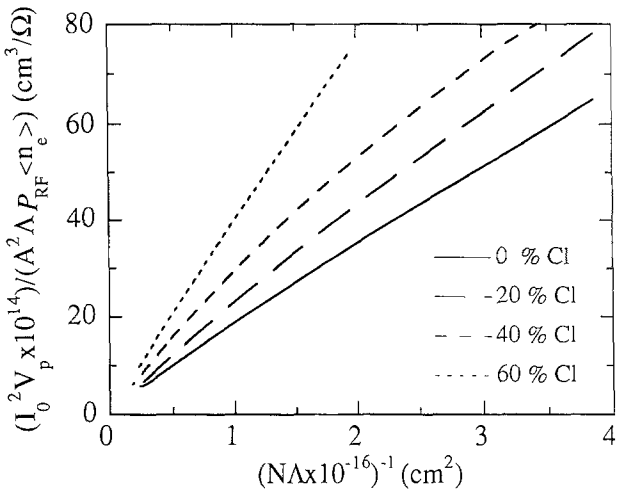

Fig. 11. $(I_0^2V_p)/(A^2\Lambda P_{RF}<n_e>)$ as a function $(N\Lambda)^{-1}$.

and hence E/N required to sustain the plasma both increase at low $N\Lambda$. An important quantity which is needed to calculate the rate of production of etchant species in the neutral transport and reaction model is the time-averaged $<k_d n_e>$ given by

$$<k_d n_e> = \frac{1}{T}\int_t^{t+T} n_e k_d (E/N, y_i)\, dt \qquad [36]$$

Since the electron density is only slightly modulated in time one can write

$$<k_d n_e> = <k_d> <n_e> \qquad [37]$$

Comparison of the production rate found using Eq. [36] and Eq. [37] showed that Eq. [37] is an excellent approximation (less than 1% error). Equations similar to Eq. [37] can also be written for other electron impact reaction coefficients such as ionization and attachment.

In practice, use of Fig. 10-12 may require some iteration since the atomic chlorine mole fraction is generally unknown. Consider for example Fig. 12. One may first estimate the dissociation rate coefficient by assuming $y_i = 0$. One can then do a material balance to determine the atomic chlorine mole fraction and use Fig. 12 again to obtain a better estimate of the rate coefficient. It should be emphasized at this point that Fig. 9-12 are applicable for a pure chlorine plasma.

Neutral transport and reaction model.—To provide the dependence of atomic chlorine concentration on pressure and electrode spacing, Eq. [20] was solved for both first and

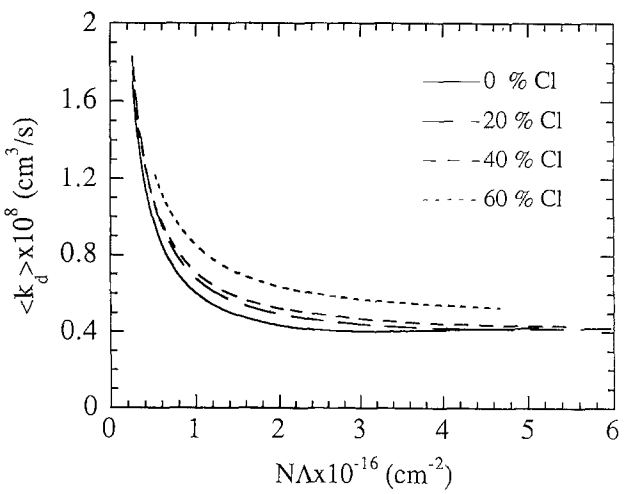

Fig. 12. Electron impact dissociation rate coefficient as a function of $N\Lambda$.

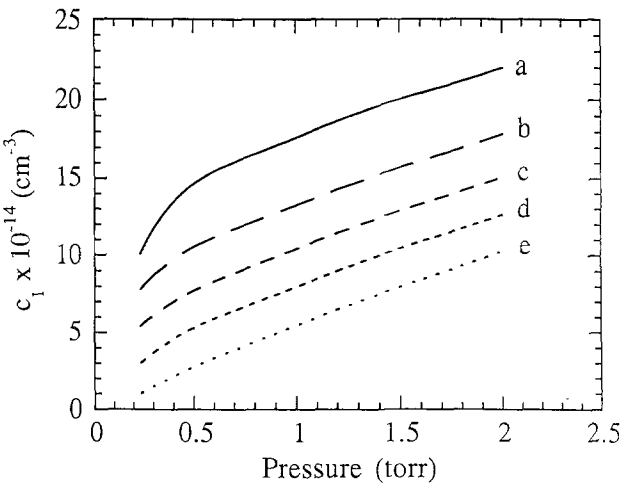

Fig. 13. Atomic chlorine concentration at the center of the reactor as a function of pressure for (a) $n = 1$, $k_{m1} = 100$ cm/s; (b) $n = 2$, $k_{m2} = 1 \times 10^{-13}$ cm^4 s^{-1}; (c) $n = 2$, $k_{m2} = 5 \times 10^{-13}$ cm^4 s^{-1}; (d) $n = 1$, $k_{m1} = 500$ cm/s; (e) diffusion limited process. Other conditions were 100 W, 25 sccm, and 1.27 cm electrode spacing.

second order surface recombination kinetics. The atomic chlorine concentration at the center of the reactor as a function of pressure is plotted in Fig. 13 for several values of the surface reaction rate coefficient. For infinitely fast surface reaction (diffusion limited process) the atomic chlorine concentration increases linearly with pressure (Curve e). The atomic chlorine concentration does not extrapolate to zero value at zero pressure because of increasing production rate with decreasing $N\Lambda$. The dependence of atomic chlorine concentration on electrode spacing for both first and second order reaction kinetics is shown in Fig. 14. The behavior is very similar to that of Fig. 13. By inspecting Fig. 13 and Fig. 14 one concludes that it is difficult to distinguish between first and second order surface recombination kinetics simply by examining the dependence of the atomic chlorine concentration on pressure or electrode spacing.

Limiting cases of the neutral transport and reaction model provide insight into the dominant transport processes in the reactor as well as the kinetics of the heterogeneous reactions. In some limiting cases convenient analytic solutions are also possible. At low flow rate and pressure, atomic chlorine loss by convection and volume recombination is relatively unimportant. For example, at 0.5 Torr, 25 sccm, 100 W, and 1.25 cm electrode spacing, the

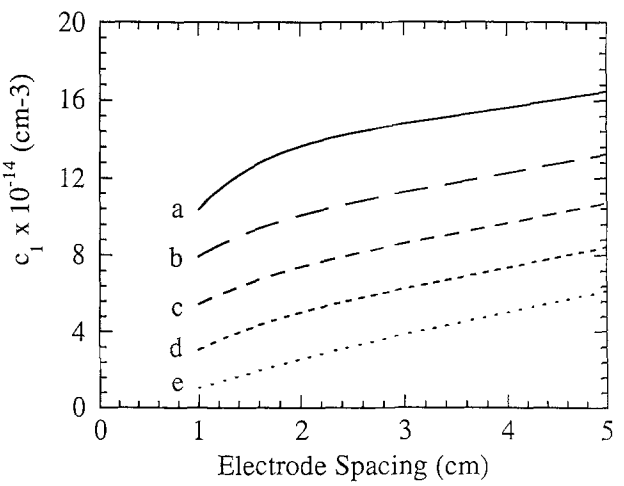

Fig. 14. Atomic chlorine concentration at the center of the reactor as a function of interelectrode spacing for (a) $n = 1$, $k_{m1} = 100$ cm/s; (b) $n = 2$, $k_{m2} = 1 \times 10^{-13}$ cm^4 s^{-1}; (c) $n = 2$, $k_{m2} = 5 \times 10^{-13}$ cm^4 s^{-1}; (d) $n = 1$, $k_{m1} = 500$ cm/s; (e) diffusion limited process. Other conditions were 100 W, 25 sccm, and 0.3 Torr.

combined loss rate by convection and volume recombination is less than 3% of the total loss rate. Under these conditions, the atomic chlorine concentration is determined by the rates of surface reaction, diffusion, and production. When convection and volume recombination are negligible, the chlorine mole fraction is less than 0.2 (so that a constant k_d can be used, see Fig. 12), and there are no radial concentration gradients in the reactor (*e.g.*, no wafer present), Eq. [20] is reduced to

$$\frac{d^2y_1}{d\zeta^2} + \frac{Da_p}{\eta^2}(1 - y_1) = 0 \qquad [38]$$

with the boundary conditions

$$\frac{dy_1}{d\zeta} = -\frac{\Phi_n}{\eta} y_1^n \quad \text{at} \quad \zeta = 1 \quad \text{and} \quad \frac{dy_1}{d\zeta} = 0 \quad \text{at} \quad \zeta = 0 \qquad [39]$$

where

$$\zeta = \frac{z}{L}; \eta = \frac{r_e}{L}; Da_p = \frac{<(2k_d + k_a)\, n_e> r_e^2}{D_1};$$

$$\Phi_n = \frac{k_n N^{n-1} r_e}{D_1} \qquad [40]$$

The Damkohler number Da_p is the ratio of the characteristic time for diffusion to the characteristic time for etchant production. The Thiele modulus Φ_n characterizes the relative importance of the wall recombination rate to the diffusive transport rate. For high values of the Thiele modulus the etchant loss process is diffusion controlled.

For first order heterogeneous reaction ($n = 1$) the solution to Eq. [38] and Eq. [39] is given by

$$y_1 = 1 - \frac{\cosh\left(\sqrt{\frac{Da_p}{\eta^2}}\zeta\right)}{\frac{\sqrt{Da_p}}{\Phi_1}\sinh\left(\sqrt{\frac{Da_p}{\eta^2}}\right) + \cosh\left(\sqrt{\frac{Da_p}{\eta^2}}\right)} \qquad [41]$$

For second order heterogeneous reaction (n=2) the atomic chlorine mole fraction as a function of axial position can be obtained from

$$y_1 = 1 - \frac{1}{2}\left(B - \sqrt{B^2 - 4\,\mathrm{sech}^2\left(\sqrt{\frac{Da_p}{\eta^2}}\right)}\right) \cosh\left(\sqrt{\frac{Da_p}{\eta^2}}\zeta\right) \qquad [42]$$

where

$$B = \left(2 + \frac{\sqrt{Da_p}}{\Phi_2}\tanh\left(\sqrt{\frac{Da_p}{\eta^2}}\right)\right)\mathrm{sech}\left(\sqrt{\frac{Da_p}{\eta^2}}\right) \qquad [43]$$

For infinitely fast surface recombination reaction ($\Phi_1 \to \infty$ or $\Phi_2 \to \infty$) both Eq. [41] and Eq. [42] reduce further to

$$y_1 = 1 - \frac{\cosh\left(\sqrt{\frac{Da_p}{\eta^2}}\zeta\right)}{\cosh\left(\sqrt{\frac{Da_p}{\eta^2}}\right)} \qquad [44]$$

Equation [44] gives the atomic chlorine mole fraction when surface recombination of Cl is limited by diffusion to the electrodes. Hence the result does not depend on the heterogeneous reaction rate coefficient.

The above equations give the atomic chlorine mole fraction for different values of the relevant dimensionless groups. It is therefore instructive to investigate the dependence of these dimensionless groups on the externally controlled reactor operating variables such as pressure, power, and electrode spacing. The Damkohler number for etchant production Da_p (see Eq. [40]) for example, may be written as

$$Da_p = \frac{2\,F_4(N\Lambda)\,F_2(N\Lambda)\,<P_{RF}>\Lambda\, r_e^2}{D_1 V_p} \qquad [45]$$

In Eq. [45], $F_2(N\Lambda)$ is given by Eq. [34] and Fig. 10, and $<k_d> = F_4(N\Lambda)$ is shown in Fig. 12. Thur, for given $<P_{RF}>$, N, r_e, and L, Da_p may be found using Eq. [45]. Then, for known surface reaction rate coefficient, the Cl concentration profile may be obtained using Eq. [41] or Eq. [42].

For first order kinetics, Eq. [41] can be used to evaluate the atomic chlorine mole fraction at the reactor center (at $\zeta = 0$). Expanding the hyperbolic functions in Taylor series and retaining only the first two terms and introducing dimensional quantities one can obtain

$$y_1\Big|_{\zeta=0} \cong \frac{F_2(N\Lambda)F_4(N\Lambda)\,<P_{RF}>\Lambda}{\pi r_e^2}\left(\frac{1}{k_1} + \frac{L}{2D_1}\right) \qquad [46]$$

It turns out that the product $F_2(N\Lambda)\,F_4(N\Lambda)$ is approximately proportional to $(N\Lambda)^{-1}$. For infinitely fast surface reaction ($k_1 \to \infty$), the second term inside the brackets on the right hand side of Eq. [46] dominates, and the atomic chlorine concentration depends linearly on pressure and interelectrode spacing (see also Fig. 13 and 14). As the interelectrode spacing changes the production rate varies as L^{-1}, while the diffusion rate varies as L^{-2}. Hence, for a diffusion-controlled process the net result is an increase in atomic chlorine concentration with increasing spacing.

Equation [46] shows that the atomic chlorine concentration c_1 should increase linearly with RF power for first order recombination kinetics. It can be shown that c_1 should increase as the square root of RF power for second order kinetics. This suggests a method for exploring the order of the surface reaction using the experimentally measured atomic chlorine concentration as a function of power. However, complications such as change of the plasma radius as the power is varied make it difficult to extract kinetic information from the experimental measurements of c_1 as a function of power. This point will be further addressed in Part II.

Summary and Conclusions

A comprehensive mathematical model of the chlorine plasma etching of polysilicon was developed. An electron kinetics model of the bulk plasma was coupled to the Boltzmann transport equation to predict key internal plasma properties such as the electron density and energy, electron impact reaction rate coefficients, the current flowing through the plasma, and the self-sustained electric field to neutral density ratio. These key plasma properties were then used in an etchant transport and reaction model to predict the atomic chlorine concentration in the reactor. Emphasis was placed on the methodology, so that similar approaches can be used to model other plasma systems. In the present work, the case of an empty reactor (no polysilicon film present) was examined. The case of polysilicon etching and uniformity will be examined in future publications.

The calculated electron energy distribution function was nonMaxwellian. The mean electron energy increased monotonically with increasing atomic chlorine mole fraction y_1 in the reactor, whereas the electron characteristic energy was rather insensitive to y_1. In the range of E/N of interest, the electron impact reaction rate coefficients were found to increase exponentially with E/N.

Several key internal plasma properties were combined in groups which were a function of $N\Lambda$ only. In this way, the results of the bulk plasma model were reduced to a few unified plots which relate the electron density and energy, self-sustained electric field, peak current, and electron impact reaction rate coefficients to reactor operating parameters (pressure, power, and reactor geometry). For values of $N\Lambda > 2 \times 10^{16}$ cm^{-2}, the electron impact reaction rate coefficients were insensitive to $N\Lambda$. For lower values of $N\Lambda$, these rate coefficients increased with decreasing $N\Lambda$. The results of the unified plots are useful in transport and reac-

tion models of the chlorine plasma, since the electron properties and electron reaction rate coefficients can be calculated from first principles and there is no need to treat these important quantities as adjustable parameters.

The atomic chlorine concentration in the reactor was calculated using different heterogeneous recombination kinetics. The atomic chlorine concentration showed similar dependence on pressure and electrode spacing for either first or second order surface recombination kinetics. Analytic expressions for the atomic chlorine mole fraction were derived for simplified cases. The atomic chlorine concentration increased linearly with RF power for first order surface recombination reaction, and was proportional to the square root of power for second order recombination reaction.

The assumptions introduced in the model reduce the parameter range over which the model is applicable. Specifically, the model is applicable at intermediate frequencies (≈3-15 MHz), above the ion plasma frequency but below the electron energy relaxation frequency, and at relatively high pressures (>0.25 Torr) for which the continuum approximation is valid and secondary electron effects are unimportant. Further refinements of the model should include an improved sheath model applicable to electronegative plasmas, and an energy balance to compute the gas and wafer temperatures.

In order to improve their predictive capability, transport and reaction models of plasma reactors must account for the variation of key plasma properties (electron energy and density, ion bombardment flux and energy, etc.) as a function of reactor geometry and operating conditions. One approach towards that end is to integrate the glow discharge models (38) with the etchant transport and reaction models. This approach is computationally unfeasible at the present time, especially since the development of two dimensional RF discharge models is still at its infancy (10). A different approach was taken in the present work by splitting the glow discharge model into bulk plasma and sheath models. Comparison of the results given by the two different approaches will be presented elsewhere.

Acknowledgments

The authors are grateful to the National Science Foundation (CBT 8708908). Texas Instruments, the Welch Foundation, and the Texas Higher Education Coordinating Board (Texas Advanced Research Program) for financial support of this work.

Manuscript submitted March 28, 1991; revised manuscript received Jan. 20, 1992.

The University of Houston assisted in meeting the publication costs of this article.

LIST OF SYMBOLS

A	electrode area, cm^2
c	species concentration, cm^{-3}
Co	collision number
D	diffusion coefficient, cm^2/s
D_{ae}	electron ambipolar diffusion coefficient, cm^2/s
Da_p	Damkohler number for production, Eq. [40]
E	electric field, V/cm
E_0	peak electric field, V/cm
E_+	ion bombardment energy, eV
e	electronic charge, 1.609×10^{-19} C
f_o	electron energy distribution function
I_0	peak current, A
I_+	ion bombardment current density, mA/cm^2
I_t	total plasma current, A
k_a	dissociative attachment reaction rate coefficient, cm^3/s
k_B	Boltzmann's constant, eV/K
k_d	molecular chlorine dissociation rate coefficient, cm^3/s
k_{i1}	atomic chlorine ionization rate coefficient, cm^3/s
k_{i2}	molecular chlorine ionization rate coefficient, cm^3/s
k_{iT}	total ionization rate coefficient, $(y_1k_{i1} + (1 - y_1)k_{i2})$, cm^3/s
k_n	nth order reaction rate coefficient, $cm^{(3n-2)}/s$
k_r	homogeneous (volume) recombination rate coefficient, cm^6/s
L	half interelectrode gap, cm
m_e	electron mass, g
m_+	ion mass, g
N	total neutral density, cm^{-3}
n_+	positive ion density, cm^{-3}
n_e	electron density, cm^{-3}
P	pressure, Torr
$<P_{RF}>$	time-averaged RF power, W
Q, Q_0	volumetric flow rate, cm^3/min, sccm
R_t	total etch rate, $cm^{-2}\ s^{-1}$
R_w	wall recombination reaction rate, $cm^{-2}\ s^{-1}$
r	radial position, cm
r_e	electrode radius, cm
r_s	shield radius, cm
r_w	wafer radius, cm
S	collision integral
T	period of the applied field, s
T_e	electron "temperature," K
T_g	gas temperature, K
t	tims, s
$\mathbf{u}$	gas velocity vector, cm/s
u	radial component of the gas velocity vector, cm/s
u_+	ion drift velocity in the sheath, cm/s
u_+	dimensionless ion drift velocity in the sheath
V_p	plasma volume, cm^3
$\mathbf{v}$	electron velocity vector, cm/s
V	dimensionless axial gas velocity
V^*	dimensionless sheath potential drop
V_s	sheath potential, V
v	axial component of the gas velocity vector, cm/s
v_d	electron drift velocity, cm/s
v_w	gas velocity at the showerhead electrode, cm/s
y	species mole fraction
z	axial position, cm

Greek symbols

ϵ	electron energy, eV
ϵ_0	vacuum permittivity, $8.854188 \times 10^{-12}\ C^2/J\text{-}m^2$
ϵ_c	characteristic electron energy, eV
ζ	dimensionless axial position
η	reactor aspect ratio
Λ	characteristic diffusion length, cm
μ	mobility, $cm^2/V\text{-}s$
υ	gas kinematic viscosity, cm^2/s
υ_a	applied excitation frequency, s^{-1}
υ_m	momentum collision frequency, s^{-1}
υ_u	electron energy relaxation frequency, s^{-1}
Φ_n	Thiele modulus for nth order reaction, Eq. [40]
ρ	gas density, g/cm^3
σ_j	collision cross section for electron impact reaction j, cm^2
τ	shear stress tensor
χ	ratio of ion density to electron density
ω	applied excitation frequency, rad/s
∇, ∇_r	gradient in x, y, z space
∇_v	gradient in velocity space

Subscripts

1	atomic chlorine
2	molecular chlorine
+	positive ions
−	negative ions
e	electrons or electrode
n	reaction order
M	third body (Reaction [R9], Table I)
rms	root mean square

REFERENCES

1. "Plasma etching: An introduction," D. M. Manos and D. L. Flamm, Editors, Academic Press Inc., New York (1989).
2. "VLSI Electronics: Microstructure Science," Vol. 8, N. G. Einspruch and D. M. Brown, Editors, Academic Press Inc., New York (1984).
3. D. L. Flamm and V. M. Donnelly, *Plasma Chem. Plasma Process.*, **1**, 317 (1981).
4. J. W. Coburn, *ibid.*, **2**, 1 (1982).
5. K. D. Allen, H. H. Sawin, M. T. Mocella, and M. W. Jenkins, *This Journal*, **133**, 2315 (1986).
6. K. D. Allen and H. H. Sawin, *ibid.*, **133**, 2326 (1986).
7. K. D. Allen, H. H. Sawin, and A. Yokozeki, *ibid.*, **133**, 2331 (1986).

8. D. B. Graves, *J. Appl. Phys.*, **62,** 88 (1987).
9. J. P. Boeuf, *Phys. Rev. A.*, **36,** 2782 (1987).
10. J. H. Tsai and C. Wu, *ibid.*, **41,** 5626 (1990).
11. M. J. Kushner, *IEEE Trans. Plasma Sci.*, **PS-14,** 188 (1986).
12. T. A. Cleland and D. W. Hess, *This Journal*, **136,** 3103 (1989).
13. M. Dalvie, K. F. Jensen, and D. B. Graves, *Chem. Eng. Sci.*, **41,** 653 (1986).
14. M. Dalvie and K. F. Jensen, *J. Vac. Sci. Technol.*, **A8,** 1648 (1990).
15. J. A. Folta and R. C. Alkire, *This Journal*, **137,** 3173 (1990).
16. A. S. Kao, and H. G. Stenger, Jr., *ibid.*, **137,** 954 (1990).
17. J. Kobayashi, N. Nakazato, and K. Kiratsuka, *ibid.*, **136,** 1781 (1989).
18. S. P. Venkatesan, I. Trachtenberg, and T. F. Edgar, *ibid.*, **137,** 2280 (1990).
19. J. Liu, L. Huppert, and H. H. Sawin, *J. Appl. Phys.*, **68,** 3916 (1990).
20. D. J. Economou, D. R. Evans, and R. C. Alkire, *This Journal*, **135,** 756 (1988).
21. L. Kline and M. J. Kushner, *Critical Reviews in Solid State and Materials Sciences*, **16,** 1 (1989).
22. D. B. Graves, *AIChE J.*, **35,** 1 (1989).
23. D. J. Economou and R. C. Alkire, *This Journal*, **135,** 2786 (1988).
24. D. J. Economou, S. K. Park, and G. D. Williams, *ibid.*, **136,** 188 (1989).
25. J. Ignacio Ulacio F. and J. P. McVittie, in "Plasma Processing" G. S. Mathad, G. C. Schwartz, and D. W. Hess, Editors, PV 88-22, p. 43, The Electrochemical Society Softbound Proceedings Series, Pennington, NJ (1988).
26. G. L. Rogoff, J. M. Kramer, and R. B. Piejak, *IEEE Trans. Plasma Sci.*, **PS-14,** 103 (1986).
27. V. M. Donnelly, D. L. Flamm, and G. Collins, *J. Vac. Sci. Technol.*, **21,** 817 (1982).
28. V. M. Donnelly, D. L. Flamm, and R. Bruce, *J. Appl. Phys.*, **58,** 2135 (1985).
29. A. D. Richards, B. E. Thompson, K. D. Allen, and H. H. Sawin, *ibid.*, **62,** 792 (1987).
30. G. S. Selwyn, L. D. Baston, and H. H. Sawin, *Appl. Phys. Lett.*, **51,** 898 (1987).
31. E. S. Aydil and D. J. Economou, *This Journal*, **139,** 1406 (1992).
32. B. E. Cherrington, "Gaseous Electronics and Gas Lasers," Pergamon Press, New York (1979).
33. M. V. Kurepa, and D. S. Belic, *J. Phys. B*, **11,** 3719 (1978).
34. P. S. Ganas, *J. Appl. Phys.*, **63,** 277 (1988).
35. W. L. Morgan, Joint Inst. for Lab. Astrophysics, Univ. of Colorado, Boulder, Rep. 19 (1979).
36. D. L. Flamm and V. M. Donnelly, *J. Appl. Phys.*, **59,** 1052 (1986).
37. D. L. Flamm, *J. Vac. Sci. Technol.*, **A4,** 729 (1986).
38. S. K. Park and D. J. Economou, *J. Appl. Phys.*, **68,** 3904 (1990).
39. G. L. Rogoff, *J. Phys. D: Appl. Phys.*, **18,** 1533 (1985).
40. R. H. Perry and C. C. Chilton, "Chemical Engineers' Handbook," Fifth Edition, p. 3-247, McGraw-Hill, New York (1973).
41. A. C. Lloyd, *Int. J. of Chemical Kinetics*, Vol. III, 39 (1971).
42. E. A. Ogryzlo, *Can. J. Chem.*, **39,** 2556 (1961).
43. M. A. A. Clyne, and D. H. Stedman, *Int. J. of Chemical Kinetics*, **39,** 2698 (1971).
44. F. Kaufman, "Chemical Reactions in Electrical Discharges," Vol. 80, American Chemical Society (1969).
45. E. S. Aydil, Ph.D. Thesis, University of Houston, 1991.
46. A. T. Bell, in "Techniques and Applications of Plasma Chemistry," J. R. Hollahan, and A. T. Bell, Editors, p. 1, John Wiley & Sons, Inc., New York (1974).

Theoretical and Experimental Investigations of Chlorine RF Glow Discharges

II. Experimental

Eray S. Aydil[1] and Demetre J. Economou

Department of Chemical Engineering, University of Houston, Houston, Texas 77204-4792

ABSTRACT

Key plasma properties of a 13.56 MHz chlorine glow discharge were measured using several plasma diagnostic techniques. Electron density and energy, self-sustained electric field, RF current flowing through the plasma, ion bombardment energy, and atomic chlorine concentration were measured as a function of reactor operating conditions. The experimental data were compared to the predictions of a plasma reactor model which included details of the bulk plasma. Good agreement between the measured and predicted values of all the above plasma properties was obtained over a range of pressure, power, and electrode spacing without adjusting any reaction rate coefficients.

In the preceding paper (hereafter to be referred to as Part I), a comprehensive plasma reactor model for a chlorine discharge was developed including details of the bulk plasma (1). The model was used to predict key internal properties of the plasma such as the electron energy distribution function, electron density, self-sustained electric field, peak RF current, ion bombardment energy, and atomic chlorine concentration profiles. These internal plasma properties directly affect the plasma etching process outcome, namely, the etch rate, uniformity, and anisotropy. In order to test the model predictions, measurement of the key internal plasma properties is necessary.

Recent advances in *in situ* plasma diagnostic techniques have contributed to basic understanding of the plasma etching process (2). Optical emission spectroscopy and laser induced fluorescence (3-6), Langmuir probe measurements (7-9), mass spectrometry (10, 11), ion bombardment flux and energy analysis (12, 13), plasma impedance analysis (14, 15), and laser interferometry (16) have all proven most useful. Each of the above plasma diagnostic techniques has its own advantages and limitations. Thus, more than one diagnostic needs to be used to obtain complementary information. In this study, a variety of plasma diagnostics were used to monitor *in situ* key internal plasma properties, and to relate observed reactor performance to changes in easily controllable and measurable external variables such as power, pressure, flow rate, and reactor geometry.

There are a number of experimental studies of the chlorine plasma. Richards *et al.* (17) measured the atomic chlorine concentration in a parallel plate reactor using optical emission actinometry and infrared absorption spectroscopy. The authors found that the atomic chlorine mole fraction varied between 0 and 0.1. Rogoff *et al.* (18) inferred the atomic chlorine concentration in a similar-type reactor

[1] Present address: AT&T Bell Laboratories, Murray Hill, NJ 07974-2070.